Solar wind ion charge state distributions and compound cross sections for solar wind charge exchange X-ray emission

Dimitra Koutroumpa

[1]LATMOS-OVSQ, CNRS, UVSQ Paris-Saclay, Sorbonne Université, 11 Boulevard d'Alembert, 78280, Guyancourt, France

Key Points:

- Individual ion abundances show strong variations per solar wind type and solar activity period.
- Calculations with broad energy band cross-sections smooth out individual variations for different solar wind types.
- Separate ion cross-sections and continuous abundance monitoring are crucial for accurate SWCX modeling and future high resolution analyses.

Corresponding author: Dimitra Koutroumpa, dimitra.koutroumpa@latmos.ipsl.fr

Abstract

Solar Wind Charge eXchange X-ray (SWCX) emission in the heliosphere and Earth's exosphere is a hard to avoid signal in soft X-ray observations of astrophysical targets. On the other hand, the X-ray imaging possibilities offered by the SWCX process has led to an increasing number of future dedicated space missions for investigating the solar wind-terrestrial interactions and magnetospheric interfaces. In both cases, accurate modelling of the SWCX emission is key to correctly interpret its signal, and remove it from observations, when needed. In this paper, we compile solar wind abundance measurements from ACE for different solar wind types, and atomic data from literature, including charge exchange cross-sections and emission probabilities, used for calculating the compound cross-section α for the SWCX X-ray emission. We calculate α values for charge-exchange with H and He, relevant to soft X-ray energy bands (0.1 - 2.0 keV) for various solar wind types and solar cycle conditions.

1 Introduction

Discovered more than 25 years ago following comet Hyakutake's X-ray observations with the Röntgen Satellite-ROSAT (Lisse et al., 1996), solar wind charge exchange X-ray (SWCX) emission is a relatively new discovery in astrophysics. Cravens (1997) interpreted the emission as the de-excitation of highly charged solar wind ions that capture electrons from the cometary neutrals. It is now established that the emission is omnipresent in the solar system, where the solar wind interacts with planetary environments, including Mars and Venus (Dennerl et al., 2002; Dennerl, 2002), the Earth (Cravens et al., 2001), Jupiter (Cravens et al., 1995; Branduardi-Raymont et al., 2007), Pluto (Lisse et al., 2017), and interstellar neutrals flowing through the heliosphere (Lallement, 2004).

SWCX emission in the Earth's magnetosphere was first acknowledged as a time variable background measured during the ROSAT All-Sky Survey (Snowden et al., 1994), and soon the correlation between the solar wind and SWCX emission was established (Dennerl et al., 1997; Freyberg, 1998; Cox, 1998; Cravens et al., 2001). In the context of astrophysical studies with ROSAT and subsequent X-ray observatories (e.g. XMM-Newton), the SWCX foreground from the geocorona and the heliosphere is a hindrance to studies of extended astrophysical sources (e.g., Kuntz, 2018). However, heliophysicists recognized in this mechanism a powerful tool for the global study of the solar wind - planet interactions (see Sibeck et al., 2018, for a review). Indeed, these emissions are propor-

tional to the solar wind ion flux and to the density of the neutral targets. The signal is therefore sensitive to variations in these quantities. In regions of solar wind plasma pileup and/or increased neutral density, such as the subsolar magnetosheath and polar cusps, the emission is enhanced, paving the way for imaging of these key regions of the Sun-Earth system (Robertson & Cravens, 2003). Several space missions currently in development will exploit SWCX imaging of plasma density structures to investigate the coupling between the solar wind and the Earth's magnetosphere, such as ESA's Solar wind Magnetosphere Ionosphere Link Explorer-SMILE mission (Branduardi-Raymont et al., 2018), and NASA's Lunar Environment heliospheric X-ray Imager (LEXI; Walsh et al., 2020).

The SWCX emission mechanism is expressed by the following reaction:

$$M + X^{q+} \rightarrow M^{+} + X^{(q-1)+*} \rightarrow M^{+} + X^{(q-1)+} + \gamma_j \tag{1}$$

where the solar wind source ion X^{q+} captures an electron from the target neutral M. This produces a new ion in an excited state $X^{(q-1)+*}$, that de-excites by emitting an X-ray photon γ_j.

The spectrum of SWCX emission is comprised of discreet spectral lines characteristic of the produced ions $X^{(q-1)+}$ (Figure 1, based on Koutroumpa et al., 2009). The X-ray flux in a given spectral line is calculated as an integral along the line-of-sight s, in units of *photons* cm^{-2} s^{-1} sr^{-1}:

$$I(\gamma_j) = \frac{1}{4\pi} \int_{s=0}^{\infty} N_M(s)\ N_{X^{q+}}(s)\ V(s)\ \sigma_{X^{q+},M}(V)\ Y_{X^{(q-1)+},j}(V)\ ds \tag{2}$$

where, $N_M(s)$ is the neutral density, $N_{X^{q+}}(s)$ is the source ion density, $V(s)$ is the ion-neutral collision relative velocity, $\sigma_{X^{q+},M}(V)$ the velocity- and species-dependent cross-section of the collision, and $Y_{X^{(q-1)+},j}(V)$ is the photon emission probability for spectral line j of the produced ion $X^{(q-1)+}$, also dependent on the velocity and neutral target species (Figure 1, and Kharchenko, 2005).

The solar wind ion density is usually expressed as a function of proton density such that $N_{X^{q+}}(s) = \left[\frac{X^{q+}}{p}\right]\ N_p(s)$, where $\left[\frac{X^{q+}}{p}\right]$ is the source ion's abundance relative to solar wind protons. In that case we may assume that the line flux is proportional to the solar wind proton flux $N_p(s)\ V(s)$, according to equation 2. It is generally admitted that the SWCX signal variability is correlated with the solar wind proton flux, especially for broad energy band measurements in the 0.1-0.3 keV energy range (Figure 1), where the

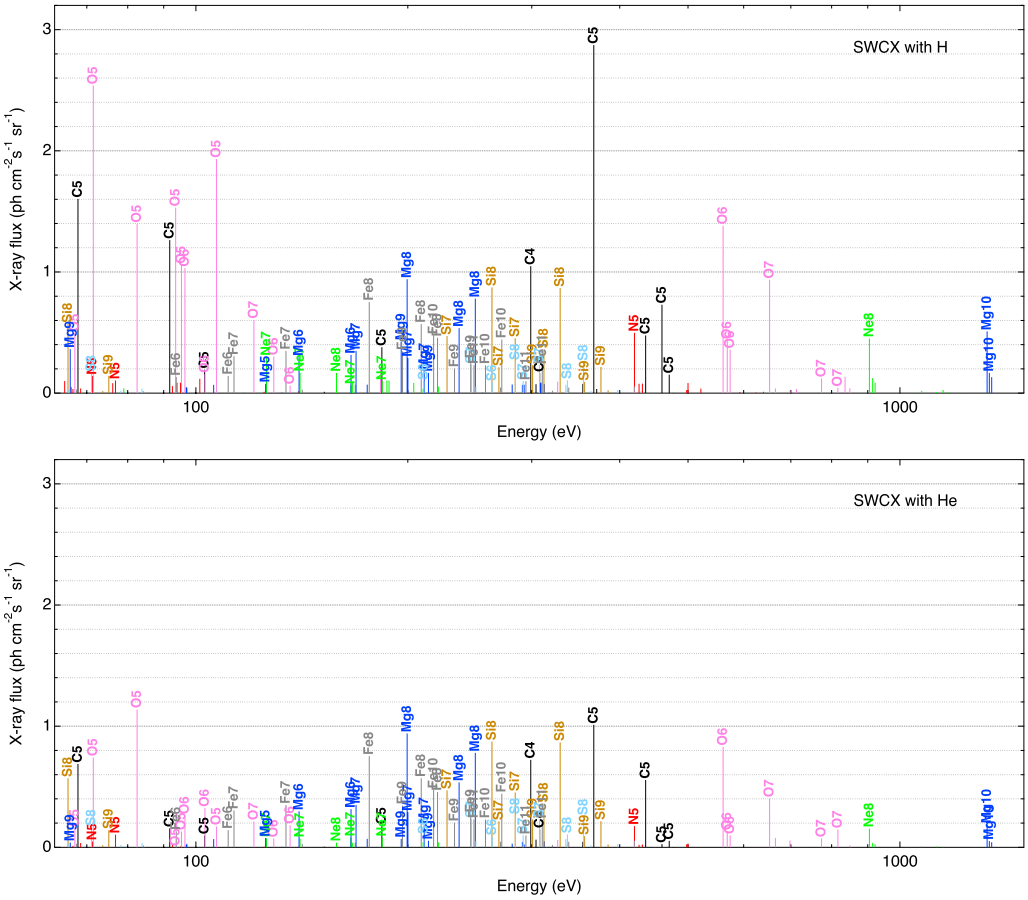

Figure 1: Theoretical X-ray spectra produced by SWCX with H (top) and He (bottom), assuming an equal column density for the two neutral targets and typical slow solar wind composition. The emitting ions $X^{(q-1)+}$ (where q refers to the ion charge state) are noted above their corresponding lines. Based on the model by Koutroumpa et al. (2009).

spectral lines are produced by a multitude of different solar wind ions (Kuntz et al., 2015). However, this is not systematically the case when studying spectral bands dominated by only a few ion species, such as oxygen (0.5-0.7 keV), as demonstrated by Kuntz et al. (2015). In several cases, SWCX enhancements were found to be sensitive to increases of ion charge-state abundances rather than, or in addition, to the overall solar wind proton flux enhancement (Snowden et al., 2004; Carter et al., 2009; Ishi et al., 2019; Y. Zhang et al., 2022).

For broad soft X-ray energy band studies with low to moderate spectral resolution, it is convenient to provide a parameter that encompasses the atomic physics parameters

(cross sections and emission probabilities) relative to every ion in the solar wind, as well as the composition properties of the later for the specific energy bands. This parameter, called α, is defined in units of $eV\ cm^2$ for SWCX with neutral target M as follows:

$$\alpha_M(V) = \sum_{X^{q+}} \sum_{\Delta E,j} \left[\frac{X^{q+}}{p}\right] \sigma_{X^{q+},M}(V) Y_{X^{(q-1)+},j}(V) E_j \tag{3}$$

where ΔE is the energy range including all spectral lines γ_j of energy E_j in units of eV (for example the SMILE/SXI band between 0.1 and 2 keV). In that case, the total X-ray energy flux in the given energy range ΔE will be the sum of all lines calculated based on equation 2, such that:

$$R(\Delta E) = \frac{1}{4\pi} \alpha_M \int_{s=0}^{\infty} N_M(s)\ N_p(s)\ V(s)\ \ ds \tag{4}$$

The α compound cross-section has been routinely used in SWCX studies, with first empirical estimates varying from $6{\times}10^{-17}$ to $6{\times}10^{-15}\ eV\ cm^2$ for photon energies above 100 eV (Cravens, 1997, 2000; Cravens et al., 2001).

Schwadron and Cravens (2000) (hereafter SC00) attempted the first detailed spectroscopic modeling of cometary SWCX emission using a detailed list of solar wind ion charge state abundances from Ulysses data separated into slow and fast wind velocities, and spectral information (rough line energies and cross-sections) based on the approximation that all ions were hydrogen-like (Wegmann et al., 1998). More detailed calculations for the heliospheric SWCX spectrum based on the SC00 abundances were produced by Pepino et al. (2004) and subsequent studies (Koutroumpa et al., 2006, 2009).

The Sun-Earth interaction models fall into several categories, and analysing their specific differences would be beyond the scope of this paper. Magnetohydrodynamic (MHD) codes, such as the Open Geospace Global Circulation Model (OpenGGCM; Raeder et al., 2001), or the Piecewise Parabolic Method with a LagRangian remap (PPMLR; Hu et al., 2007), use a fluid description for all plasma components, protons (ions) and electrons alike. These models have the advantage of providing quick computation times and increased spatial and temporal resolution to analyse the plasma dynamics in the Earth's magnetosphere. However, they cannot grasp the kinetic effects that the particles' gyromotion produce in the presence of magnetic fields. Hybrid (e.g., Latmos Hybrid Simulation-LatHyS; Modolo et al., 2016) and test-particle models (Tkachenko et al., 2021) use an approach where protons/ions are described kinetically, allowing for a better description of the kinetic effects. However, these models are more computationally intensive, and

counter this drawback with reduced spatial and/or temporal resolution, and/or reduced simulation domains.

MHD codes produce proton fluxes, then base the SWCX calculations on the proportionality to this quantity as well as the compound cross-section α as shown in equation 4 (Sun et al., 2019; Connor et al., 2021). On the other hand, test-particle models (Tkachenko et al., 2021) have the advantage to calculate the SWCX emission for every ion species individually, while being more time consuming, and less flexible in terms of temporal variability. Both approaches will be complementary to support the science return of the SMILE/SXI data. The former will allow a detailed dynamic study of the general variability of the SWCX signal, while the later approach will allow more precise spectral studies of the SWCX emission, and the effects that the dynamics of individual ions may have on the morphology of the emission around magnetospheric boundaries.

In this paper we aim to provide solar wind composition estimates for various solar wind conditions as a reference guide to SWCX spectral models, and calculate the compound cross-sections α for various energy bands to assist magnetospheric SWCX simulations. In section 2 we present updated solar wind ion composition data from the Advanced Composition Explorer (ACE; Gloeckler et al., 1998) and classify the different solar wind types according to literature, as an extension to the SC00 list. In section 3 we describe the atomic data, including velocity-dependent cross-sections and emission line probabilities. In section 4 we present the results of α for SWCX with H and He atoms in different energy bands and for the various solar wind types, and offer some conclusions in section 5.

2 Solar Wind Ion composition

The ACE satellite has been monitoring, among other quantities, the solar wind density, velocity and composition from the Lagrange L1 point since 1998.

We use the ACE/SWICS 1.1 Level 2 database[1] from which we extract the ion charge state distributions $[\frac{X^{q+}}{X}]$ and elemental abundances relevant to oxygen $[\frac{X}{O}]$, in order to calculate the ion charge state relative abundances $[\frac{X^{q+}}{O}]$, as well as the alpha (He^{++}) particle speed which is equatable with the proton speed. An anomaly that occurred in

[1] `http://www.srl.caltech.edu/ACE/ASC/level2/lvl2DATA_SWICS_SWIMS.html`

August 2011 has impacted the ACE/SWICS operations, and detailed charge-state distributions and most elemental abundances are no longer provided since that date. We use the ACE/SWEPAM Level 2 database[2] to obtain the proton parameters (density and velocity) and alpha to proton ($\frac{He^{++}}{p}$) ratio. In Figure 2 we present a number of parameters showcasing the changes in solar wind properties during the solar cycle, between 1997 and 2012.

The ACE 1.1 database provides a parameter that allows a rough classification of the solar wind type, in streamer, coronal hole (CH) and interplanetary coronal mass ejection (ICME), based on the $\frac{O^{7+}}{O^{6+}}$ ratio versus proton speed functions described by Zhao et al. (2009)[3]. However, according to von Steiger and Zurbuchen (2015) the $\frac{O^{7+}}{O^{6+}}$ ratio alone, and in particular the threshold ($\frac{O^{7+}}{O^{6+}} \leq 0.145$) employed by Zhao et al. (2009), is not appropriate to properly differentiate the streamer from CH types. Indeed, upon a closer inspection, the Zhao et al. (2009) threshold produces an abnormally large population of CH SW type with respect to the other types, which seems unrealistic at ACE's low latitudes (see Figure 1 from Zhao et al., 2009). von Steiger and Zurbuchen (2015) have demonstrated from Ulysses data that a better parameter to separate streamer from CH wind is the $\frac{O^{7+}}{O^{6+}} * \frac{C^{6+}}{C^{5+}}$ product. A threshold of $\frac{O^{7+}}{O^{6+}} * \frac{C^{6+}}{C^{5+}} \leq 0.01$, clearly identifies the CH population from the slow (streamer) solar wind (see Figure 1 from that paper). The ACE data do not show a clear bi-modal distribution as the Ulysses data (compare Figure 3-left to Figure 1 of von Steiger & Zurbuchen, 2015), presumably because the Ulysses CH population originates from higher heliolatitudes, as opposed to ACE data measured at low latitudes. This seems to agree with the analysis of J. Zhang et al. (2003), who showed that the $\frac{O^{7+}}{O^{6+}}$ of equatorial CHs seems to have a much broader range of values, compared to the polar CHs that show less scatter (see their figure 5). Even though their intrinsic coronal properties are not significantly different, equatorial CHs are less frequent, short-lived, much smaller in size from polar CHs and their flow speed is lower probably due to deceleration processes from interaction with streamer wind flows. In our case, the $\frac{O^{7+}}{O^{6+}} * \frac{C^{6+}}{C^{5+}}$ product seems to produce a more reasonable distribution of the different SW origins for low latitudes, as demonstrated by the number of CH vs streamer occurrences presented in the histograms in Figure 3-right.

[2] `https://izw1.caltech.edu/ACE/ASC/level2/lvl2DATA_SWEPAM.html`

[3] `http://www.srl.caltech.edu/ACE/ASC/level2/ssv4_l2desc.html`

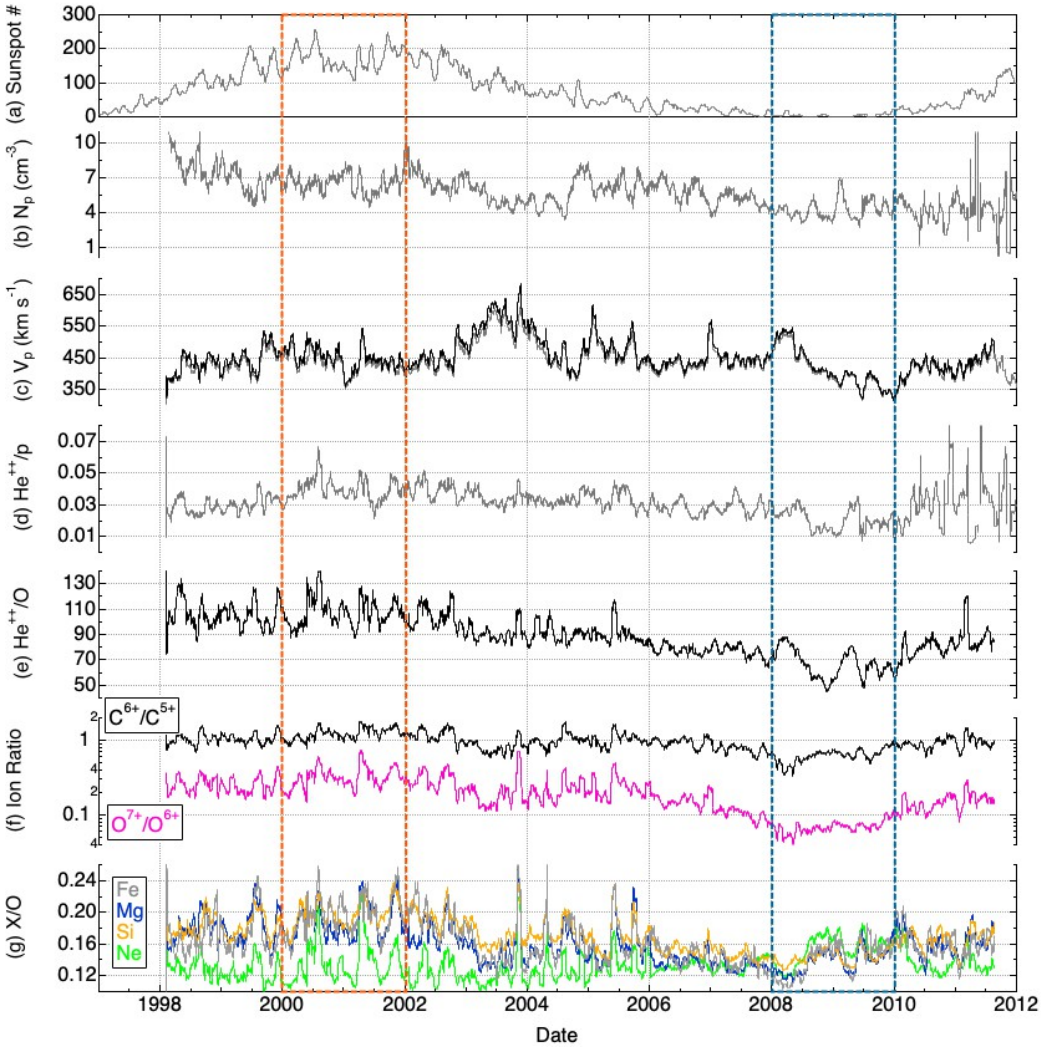

Figure 2: From top to bottom: (a) Sunspot number, (b) Proton density from SWEPAM, (c) Proton (grey) and alpha particle (black) velocities from SWEPAM and SWICS respectively, (d) alpha to proton ratio from SWEPAM, (e) alpha to oxygen ratio from SWICS, (f) Carbon (black) and Oxygen (magenta) charge state ratios, (g) Elemental abundances of the heavy ions measured with SWICS (Neon - green, Magnesium - blue, Silicon - yellow, Iron - grey). All quantities are 27-day averages. The orange and blue dashed rectangles mark out respectively the solar maximum and solar minimum limits applied in calculations (See text for details).

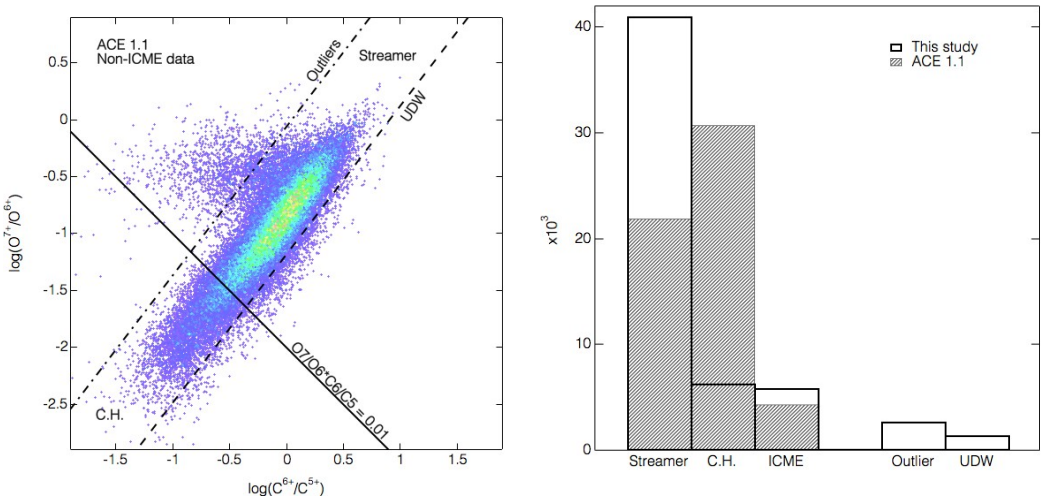

Figure 3: Left - 2D histogram of the $\log(\frac{O^{7+}}{O^{6+}})$ versus the $\log(\frac{C^{6+}}{C^{5+}})$ ratio from the non-ICME (Interplanetary Coronal Mass Ejection) ACE SWICS 1.1 data. The black lines represent the coronal hole - streamer (solid), the outlier (dot-dashed) and the Upper Depleted Wind - UDW (dashed) type separation (see text for details). Right - Comparison of the solar wind type histogram for this analysis and the ACE 1.1 website classification.

Zhao et al. (2017, 2022) have further investigated the slow solar wind, and have found two more populations that exhibit anomalous composition. The "outlier" solar wind (Zhao et al., 2017) has lower abundances for the bare ions, in particular C^{6+} (Figure 3) and is probably a signature of magnetic reconnection in its source region. The "upper depleted wind" (UDW Zhao et al., 2022), exhibits systematically depleted elemental abundances, and is most likely associated with quiet Sun regions, while the normal slow wind originates from active regions and the heliospheric current sheet streamers.

In this analysis we adopt the following classification for the solar wind type:

1. we identify ICMEs based on the list provided by Richardson and Cane (2004)[4]
2. we adopt the $\frac{O^{7+}}{O^{6+}} * \frac{C^{6+}}{C^{5+}} \leq 0.01$ threshold to identify the CH (fast) wind, and
3. we exclude the outlier and UDW slow wind populations from the streamer type.

The thresholds applied for the different populations are illustrated in Figure 3-left of the non-ICME wind population.

[4] `https://izw1.caltech.edu/ACE/ASC/DATA/level3/icmetable2.htm`

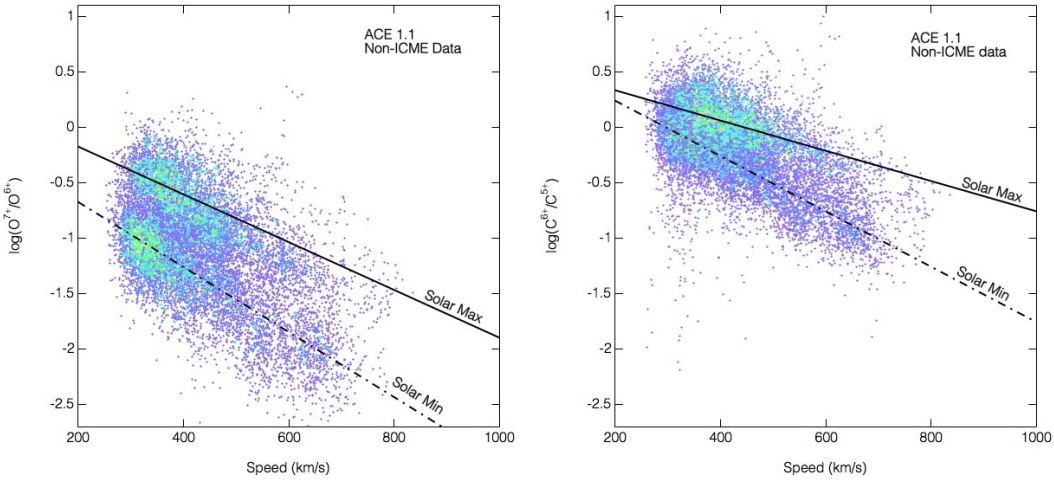

Figure 4: Left - 2D histogram of the $\log(\frac{O^{7+}}{O^{6+}})$ ratio as a function of velocity for solar maximum (2000-2002) and solar minimum (2008-2010) periods. The linear correlations for solar maximum (solid) and minimum (dot-dashed) are also overplotted, showcasing the sharp difference between the two periods. Right - Same as in the left panel, only for the $\log(\frac{C^{6+}}{C^{5+}})$ ratio versus the velocity.

It is also worth noting that ion ratios and elemental abundances in the ACE database show a significant change between solar maximum and solar minimum (see for example panels f, g of Figure 2, and Figure 4). This seems to be in agreement with previous studies showing that the 2008-2010 minimum exhibited peculiar properties such as cooler temperatures (Issautier et al., 2008) that may explain the depleted ion abundances (Lepri et al., 2013). We therefore decide to add an additional separation in solar maximum and solar minimum periods to test for changes of the compound cross section results.

The detailed results per solar wind type and solar period for solar wind He^{++} density and velocity, elemental and charge-state abundances, are given in Tables 1 and 2. The uncertainties of the measures are determined as the dispersion (width) at half maximum of the histogram distributions used to calculate the mode values per solar wind type.

The elemental abundances (Table 1) calculated for the full ACE database span for streamer and CH populations are consistent with the most recent analysis of the Ulysses data (Table 1 in von Steiger & Zurbuchen, 2015), based on the same $\frac{O^{7+}}{O^{6+}} * \frac{C^{6+}}{C^{5+}}$ threshold. A detailed comparison with the analyses of Zhao et al. (2017) and Zhao et al. (2022)

did not seem relevant, since the streamer/CH separation is not based on the same criteria. The elemental abundances are systematically depleted for CH wind, except in the case of carbon, which is more abundant in this type of wind. For most quantities, the solar maximum values are enhanced compared to solar minimum. The change is particularly sharp in the He^{++} properties (density and ratio to oxygen), as well as the $\frac{O^{7+}}{O^{6+}}$ values. Notable exceptions are the C/O and Ne/O abundances that show an increasing trend between solar maximum to solar minimum. The maximum to minimum trends we find agree with the analysis of Lepri et al. (2013) of the ACE 1.1 database for the same periods.

Changes from maximum to minimum are also noticeable in some charge-state abundance ratios (Table 2), with the highest charge states showing a decreasing trend, while the lower charge states, such as Ne^{8+}, and the heavier metals ($Mg^{7+,6+}$, $Si^{8+,7+}$, $Fe^{9+,8+,7+}$) seem more abundant during solar minimum, particularly for CH solar wind type. However, these trends should be considered with caution, due to the lower statistics of the ACE data during solar minimum.

In Figure 5 we plot the ACE 1.1 to the SC00 charge state abundance ratio for the streamer (slow) and CH (fast) populations, for the complete database, as well as for the maximum and minimum periods. We also plot indicatively the error-bars for the complete database values (we omit the error-bars for the solar maximum and minimum periods so as to not overcrowd the plot). SC00 did not provide any uncertainties, thus the plotted error-bars are proportional to the uncertainties of the ACE 1.1 charge state abundances from Table 2, and showcase the scatter of the measures. In general the ACE data are somewhat lower than the SC00 Ulysses values, except for the lower charge states of Mg, Si and Fe in the CH wind. The ACE data during solar maximum are a closer match to the SC00 values, especially for the same heavier metals (Mg, Si, Fe) in the CH type wind. This may be due to the fact that the Ulysses data used in SC00 spanned the period around solar maximum. It should be noted though, that the slow and fast selection in the SC00 study was based on a velocity threshold in contrast to the present analysis were we use the $\frac{O^{7+}}{O^{6+}} * \frac{C^{6+}}{C^{5+}}$ product. It would have been interesting to compare the 2008-2010 charge state abundances from Ulysses with the corresponding ACE values, but unfortunately the detailed charge-state measurements in the Ulysses final archive are not available.

Table 1: Alpha particle parameters and element abundance ratios from ACE 1.1 database for streamer (Slow), CH (fast) and ICME solar wind for different solar activity periods. The uncertainties represent the dispersion of the measures at half maximum of the distribution.

	Full period (1998-2011)			Max (2000-2002)			Min (2008-2010)		
	Str.	CH	ICME	Str.	CH	ICME	Str.	CH	ICME
n_{He} (cm^{-3})	$0.148\ ^{+0.226}_{-0.091}$	$0.122^{+0.113}_{-0.058}$	$0.166\ ^{+0.328}_{-0.112}$	$0.189^{+0.203}_{-0.099}$	$0.157^{+0.127}_{-0.068}$	$0.179^{+0.315}_{-0.112}$	$0.059^{+0.128}_{-0.041}$	$0.081^{+0.097}_{-0.044}$	$0.057^{+0.099}_{-0.036}$
V_{He} (km s^{-1})	$384.7^{+114.0}_{-88}$	$610.5^{+107.6}_{-91.5}$	$422.3\ ^{+118.1}_{-92.3}$	$396.9\ ^{+104.0}_{-82.4}$	$634.\ ^{+136.0}_{-112.0}$	$429.9^{+125.5}_{-97.1}$	$340.7^{+70.6}_{-58.5}$	$551.3^{+127.7}_{-103.7}$	$345.1^{+54.4}_{-45.0}$
He/O	$87.4\ ^{+34.0}_{-24.1}$	$80.0^{+16.6}_{-13.7}$	$86.3^{+51.3}_{-32.2}$	$99.4^{+28.1}_{-21.9}$	$81.0^{+12.0}_{-10.5}$	$96.0^{+45.4}_{-30.8}$	$49.9^{+37.7}_{-21.5}$	$74.8^{+24.1}_{-18.2}$	$52.8\ ^{+24.8}_{-16.9}$
C/O	$0.620^{+0.078}_{-0.069}$	$0.651^{+0.055}_{-0.051}$	$0.599^{+0.144}_{-0.116}$	$0.615^{+0.078}_{-0.069}$	$0.642^{+0.040}_{-0.038}$	$0.592^{+0.140}_{-0.113}$	$0.626^{+0.092}_{-0.081}$	$0.635^{+0.069}_{-0.063}$	$0.608\ ^{+0.110}_{-0.093}$
Ne/O	$0.111^{+0.041}_{-0.030}$	$0.103^{+0.028}_{-0.022}$	$0.127^{+0.054}_{-0.038}$	$0.104^{+0.034}_{-0.026}$	$0.090^{+0.022}_{-0.017}$	$0.122^{+0.053}_{-0.037}$	$0.142^{+0.052}_{-0.038}$	$0.117^{+0.024}_{-0.020}$	$0.142^{+0.039}_{-0.031}$
Mg/O	$0.134^{+0.052}_{-0.037}$	$0.099^{+0.023}_{-0.019}$	$0.159^{+0.078}_{-0.052}$	$0.147^{+0.059}_{-0.042}$	$0.104^{+0.023}_{-0.019}$	$0.170^{+0.075}_{-0.052}$	$0.125^{+0.048}_{-0.035}$	$0.099^{+0.027}_{-0.021}$	$0.128^{+0.049}_{-0.035}$
Si/O	$0.151^{+0.052}_{-0.039}$	$0.123^{+0.023}_{-0.020}$	$0.169^{+0.066}_{-0.047}$	$0.172^{+0.060}_{-0.045}$	$0.123^{+0.032}_{-0.026}$	$0.185^{+0.067}_{-0.049}$	$0.133^{+0.044}_{-0.033}$	$0.119^{+0.024}_{-0.020}$	$0.132^{+0.052}_{-0.037}$
Fe/O	$0.121^{+0.071}_{-0.045}$	$0.092^{+0.024}_{-0.019}$	$0.127^{+0.096}_{-0.055}$	$0.136^{+0.077}_{-0.049}$	$0.096^{+0.035}_{-0.026}$	$0.145^{+0.107}_{-0.062}$	$0.108^{+0.067}_{-0.041}$	$0.092\ ^{+0.025}_{-0.019}$	$0.109^{+0.066}_{-0.041}$
O^{7+}/O^{6+}	$0.131^{+0.210}_{-0.080}$	$0.020^{+0.017}_{-0.009}$	$0.317^{+0.585}_{-0.204}$	$0.180^{+0.291}_{-0.110}$	$0.029^{+0.010}_{-0.007}$	$0.353\ ^{+0.548}_{-0.218}$	$0.073^{+0.069}_{-0.036}$	$0.015^{+0.016}_{-0.008}$	$0.103^{+0.068}_{-0.038}$
C^{6+}/C^{5+}	$0.859^{+0.876}_{-0.420}$	$0.187^{+0.124}_{-0.076}$	$1.291^{+1.560}_{-0.718}$	$0.990^{+0.956}_{-0.498}$	$0.196^{+0.071}_{-0.051}$	$1.354^{+1.497}_{-0.711}$	$0.654^{+0.443}_{-0.263}$	$0.176^{+0.160}_{-0.081}$	$0.797^{+0.433}_{-0.286}$

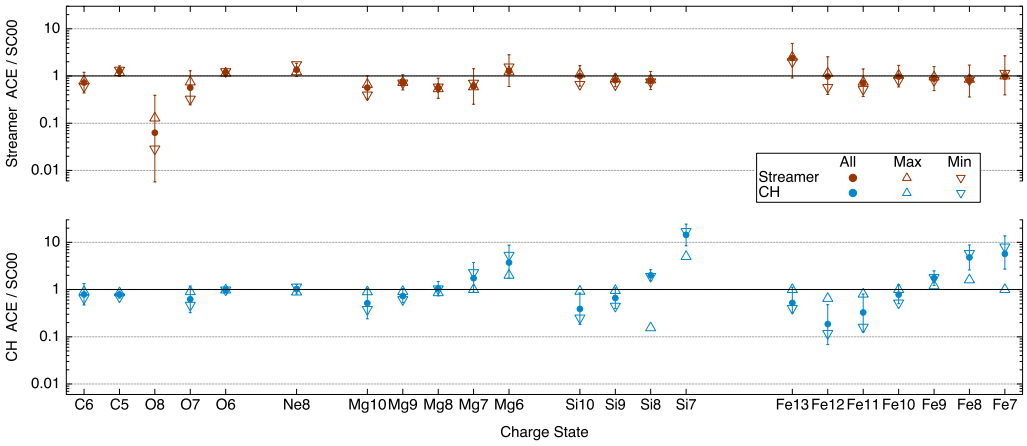

Figure 5: Ratio of the ACE 1.1 / SC00 charge-state abundances for the complete 1998-2011 period (full circles), the solar maximum period (upward triangles) and solar minimum period (downward triangles), for the streamer (top panel - dark red) and CH (bottom panel - blue) solar wind types. Error-bars are provided for the complete database values only so as to not overcrowd the plot.

Table 2: Charge state abundance ratios relative to oxygen $\frac{X^{q+}}{O}$ from ACE 1.1 database for streamer (Slow), CH (fast) and ICME solar wind for different solar activity periods.The uncertainties represent the dispersion of the measures at half maximum of the distribution.

	Full period (1998-2011)			Max (2000-2002)			Min (2008-2010)		
Ion	Str.	CH	ICME	Str.	CH	ICME	Str.	CH	ICME
C^{6+}	$0.231^{+0.151}_{-0.092}$	$0.067^{+0.047}_{-0.027}$	$0.291\ ^{+0.232}_{-0.130}$	$0.250^{+0.1604}_{-0.095}$	$0.077\ ^{+0.026}_{-0.021}$	$0.296^{+0.221}_{-0.126}$	$0.191^{+0.120}_{-0.068}$	$0.056^{+0.051}_{-0.027}$	$0.215^{+0.126}_{-0.074}$
C^{5+}	$0.269^{+0.076}_{-0.064}$	$0.344^{+0.066}_{-0.054}$	$0.221^{+0.100}_{-0.071}$	$0.248^{+0.085}_{-0.064}$	$0.377^{+0.048}_{-0.043}$	$0.207^{+0.094}_{-0.062}$	$0.280^{+0.053}_{-0.044}$	$0.308^{+0.049}_{-0.047}$	$0.270^{+0.052}_{-0.042}$
$N^{7+(a)}$	0.006	0.000							
$N^{6+(a)}$	0.058	0.011							
$N^{5+(a)}$	0.065	0.127							
O^{8+}	$0.004^{+0.023}_{-0.004}$	<0.001	$0.028^{+0.191}_{-0.025}$	$0.009^{+0.051}_{-0.007}$	<0.001	$0.037^{+0.178}_{-0.031}$	$0.002^{+0.005}_{-0.001}$	<0.001	$0.002^{+0.007}_{-0.002}$
O^{7+}	$0.113^{+0.145}_{-0.064}$	$0.019^{+0.017}_{-0.009}$	$0.237^{+0.174}_{-0.102}$	$0.149^{+0.162}_{-0.080}$	$0.027^{+0.010}_{-0.008}$	$0.245^{+0.170}_{-0.098}$	$0.065^{+0.058}_{-0.030}$	$0.014^{+0.015}_{-0.007}$	$0.088^{+0.050}_{-0.033}$
O^{6+}	$0.874^{+0.070}_{-0.071}$	$0.953^{+0.013}_{-0.009}$	$0.764^{+0.180}_{-0.142}$	$0.832\ ^{+0.111}_{-0.101}$	$0.946^{+0.020}_{-0.002}$	$0.727^{+0.175}_{-0.146}$	$0.904^{+0.040}_{-0.044}$	$0.952^{+0.014}_{-0.009}$	$0.887^{+0.056}_{-0.047}$
O^{5+}	$0.019^{+0.009}_{-0.006}$	$0.025^{+0.009}_{-0.007}$	$0.016^{+0.010}_{-0.006}$	$0.017^{+0.008}_{-0.005}$	$0.020^{+0.006}_{-0.005}$	$0.015^{+0.008}_{-0.005}$	$0.024^{+0.012}_{-0.008}$	$0.027\ ^{+0.010}_{-0.007}$	$0.024^{+0.012}_{-0.008}$
Ne^{9+}	$0.003^{+0.007}_{-0.002}$	$0.001^{+0.002}_{-0.001}$	$0.008^{+0.033}_{-0.007}$	$0.003^{+0.008}_{-0.002}$	$0.001\ ^{+0.001}_{-0.001}$	$0.008^{+0.033}_{-0.007}$	$0.003^{+0.006}_{-0.002}$	$0.001^{+0.002}_{-0.001}$	$0.003^{+0.006}_{-0.002}$
Ne^{8+}	$0.114^{+0.043}_{-0.032}$	$0.105^{+0.026}_{-0.023}$	$0.128^{+0.044}_{-0.034}$	$0.103\ ^{+0.032}_{-0.026}$	$0.09^{+0.022}_{-0.016}$	$0.122^{+0.048}_{-0.033}$	$0.146^{+0.059}_{-0.039}$	$0.116^{+0.025}_{-0.019}$	$0.142^{+0.044}_{-0.030}$
Mg^{12+}	<0.001	0.000	$0.001^{+0.002}_{-0.001}$	<0.001	0.000	$0.001^{+0.003}_{-0.001}$	0.000	0.000	$0.001^{+0.001}_{-0.001}$
Mg^{11+}	$0.001^{+0.001}_{-0.001}$	<0.001	$0.001^{+0.008}_{-0.001}$	$0.001^{+0.001}_{-0.001}$	0.000	$0.001^{+0.009}_{-0.001}$	$0.001^{+0.001}_{-0.001}$	<0.001	$0.001^{+0.001}_{-0.001}$
Mg^{10+}	$0.055^{+0.043}_{-0.024}$	$0.015^{+0.016}_{-0.008}$	$0.088^{+0.078}_{-0.042}$	$0.065^{+0.043}_{-0.026}$	$0.026^{+0.011}_{-0.008}$	$0.095^{+0.076}_{-0.043}$	$0.039^{+0.035}_{-0.018}$	$0.011^{+0.011}_{-0.005}$	$0.046^{+0.035}_{-0.020}$
Mg^{9+}	$0.038^{+0.017}_{-0.012}$	$0.032^{+0.014}_{-0.009}$	$0.040^{+0.018}_{-0.013}$	$0.038^{+0.017}_{-0.012}$	$0.040^{+0.012}_{-0.011}$	$0.039^{+0.019}_{-0.012}$	$0.037\ ^{+0.021}_{-0.014}$	$0.027^{+0.014}_{-0.009}$	$0.038^{+0.024}_{-0.015}$

manuscript accepted in *SMILE Special Issue - Earth and Planetary Physics*

Mg^{8+}	$0.023^{+0.014}_{-0.009}$	$0.030^{+0.012}_{-0.009}$	$0.020^{+0.014}_{-0.008}$	$0.022^{+0.014}_{-0.009}$	$0.023^{+0.011}_{-0.008}$	$0.020^{+0.014}_{-0.008}$	$0.024^{+0.017}_{-0.009}$	$0.029^{+0.012}_{-0.008}$	$0.023^{+0.019}_{-0.010}$
Mg^{7+}	$0.010^{+0.014}_{-0.006}$	$0.012^{+0.014}_{-0.006}$	$0.009^{+0.012}_{-0.005}$	$0.010^{+0.013}_{-0.006}$	$0.007^{+0.009}_{-0.004}$	$0.008^{+0.010}_{-0.005}$	$0.012^{+0.017}_{-0.007}$	$0.016^{+0.014}_{-0.007}$	$0.013^{+0.016}_{-0.007}$
Mg^{6+}	$0.011^{+0.014}_{-0.006}$	$0.011^{+0.015}_{-0.006}$	$0.009^{+0.012}_{-0.005}$	$0.011^{+0.012}_{-0.006}$	$0.006^{+0.009}_{-0.004}$	$0.008^{+0.010}_{-0.005}$	$0.014^{+0.018}_{-0.008}$	$0.016^{+0.015}_{-0.008}$	$0.015^{+0.019}_{-0.009}$
Si^{12+}	$0.006^{+0.015}_{-0.004}$	$0.001^{+0.002}_{-0.001}$	$0.021^{+0.065}_{-0.016}$	$0.008^{+0.021}_{-0.006}$	$0.001^{+0.002}_{-0.001}$	$0.025^{+0.074}_{-0.018}$	$0.003^{+0.005}_{-0.002}$	$0.001^{+0.001}_{-0.001}$	$0.003^{+0.008}_{-0.002}$
Si^{11+}	$0.016^{+0.016}_{-0.008}$	$0.005^{+0.005}_{-0.002}$	$0.029^{+0.035}_{-0.016}$	$0.019^{+0.017}_{-0.009}$	$0.008^{+0.006}_{-0.003}$	$0.031^{+0.034}_{-0.016}$	$0.010^{+0.011}_{-0.005}$	$0.003^{+0.004}_{-0.002}$	$0.011^{+0.012}_{-0.006}$
Si^{10+}	$0.021^{+0.014}_{-0.008}$	$0.010^{+0.011}_{-0.005}$	$0.025^{+0.014}_{-0.009}$	$0.023^{+0.011}_{-0.008}$	$0.022^{+0.009}_{-0.006}$	$0.025^{+0.012}_{-0.009}$	$0.014^{+0.013}_{-0.007}$	$0.006^{+0.005}_{-0.003}$	$0.016^{+0.012}_{-0.007}$
Si^{9+}	$0.040^{+0.014}_{-0.011}$	$0.030^{+0.019}_{-0.012}$	$0.039^{+0.019}_{-0.013}$	$0.043^{+0.013}_{-0.010}$	$0.043^{+0.013}_{-0.010}$	$0.040^{+0.018}_{-0.012}$	$0.032^{+0.017}_{-0.011}$	$0.020^{+0.010}_{-0.006}$	$0.031^{+0.016}_{-0.010}$
Si^{8+}	$0.045^{+0.026}_{-0.016}$	$0.044^{+0.014}_{-0.010}$	$0.038^{+0.031}_{-0.017}$	$0.047^{+0.030}_{-0.018}$	$0.034^{+0.017}_{-0.010}$	$0.038^{+0.034}_{-0.018}$	$0.043^{+0.021}_{-0.014}$	$0.042^{+0.012}_{-0.010}$	$0.043^{+0.022}_{-0.014}$
Si^{7+}	$0.022^{+0.023}_{-0.012}$	$0.029^{+0.020}_{-0.012}$	$0.015^{+0.024}_{-0.009}$	$0.021^{+0.025}_{-0.011}$	$0.010^{+0.009}_{-0.005}$	$0.016^{+0.023}_{-0.009}$	$0.027^{+0.024}_{-0.012}$	$0.034^{+0.016}_{-0.011}$	$0.026^{+0.022}_{-0.012}$
Si^{6+}	$0.004^{+0.008}_{-0.003}$	$0.006^{+0.011}_{-0.004}$	$0.003^{+0.006}_{-0.002}$	$0.004^{+0.007}_{-0.002}$	$0.002^{+0.003}_{-0.001}$	$0.003^{+0.005}_{-0.002}$	$0.006^{+0.008}_{-0.003}$	$0.010^{+0.009}_{-0.004}$	$0.006^{+0.009}_{-0.004}$
$S^{11+(a)}$	0.000	0.001							
$S^{10+(a)}$	0.005	0.008							
$S^{9+(a)}$	0.016	0.027							
$S^{8+(a)}$	0.019	0.023							
$S^{7+(a)}$	0.006	0.005							
Fe^{20+}	<0.001	0.000	<0.001	<0.001	0.000	<0.001	<0.001	0.000	<0.001
Fe^{19+}	<0.001	<0.001	$0.001^{+0.002}_{-0.001}$	<0.001	<0.001	$0.001^{+0.002}_{-0.001}$	<0.001	<0.001	<0.001
Fe^{18+}	<0.001	<0.001	$0.001^{+0.002}_{-0.001}$	<0.001	<0.001	$0.001^{+0.003}_{-0.001}$	$0.001^{+0.001}_{-0.001}$	<0.001	$0.001^{+0.001}_{-0.001}$
Fe^{17+}	$0.001^{+0.001}_{-0.001}$	<0.001	$0.002^{+0.006}_{-0.001}$	$0.001^{+0.001}_{-0.001}$	<0.001	$0.002^{+0.007}_{-0.001}$	$0.001^{+0.001}_{-0.001}$	<0.001	$0.001^{+0.001}_{-0.001}$
Fe^{16+}	$0.001^{+0.003}_{-0.001}$	$0.001^{+0.001}_{-0.001}$	$0.006^{+0.043}_{-0.005}$	$0.002^{+0.005}_{-0.001}$	$0.001^{+0.00}_{-0.001}$	$0.008^{+0.058}_{-0.007}$	$0.001^{+0.002}_{-0.001}$	$0.001^{+0.001}_{-0.001}$	$0.001^{+0.002}_{-0.001}$

manuscript accepted in *SMILE Special Issue - Earth and Planetary Physics*

Fe^{15+}	$0.002^{+0.003}_{-0.001}$	$0.001^{+0.001}_{-0.001}$	$0.005^{+0.015}_{-0.004}$	$0.002^{+0.004}_{-0.001}$	$0.001^{+0.001}_{-0.001}$	$0.005^{+0.018}_{-0.004}$	$0.002^{+0.003}_{-0.001}$	$0.001^{+0.001}_{-0.001}$	$0.002^{+0.003}_{-0.001}$
Fe^{14+}	$0.004^{+0.004}_{-0.002}$	$0.002^{+0.002}_{-0.001}$	$0.006^{+0.009}_{-0.004}$	$0.004^{+0.004}_{-0.002}$	$0.003^{+0.002}_{-0.001}$	$0.006^{+0.009}_{-0.004}$	$0.003^{+0.004}_{-0.002}$	$0.002^{+0.002}_{-0.001}$	$0.003^{+0.004}_{-0.002}$
Fe^{13+}	$0.005^{+0.005}_{-0.003}$	$0.003^{+0.003}_{-0.001}$	$0.008\ ^{+0.011}_{-0.005}$	$0.005^{+0.006}_{-0.003}$	$0.005^{+0.004}_{-0.002}$	$0.007^{+0.012}_{-0.005}$	$0.004^{+0.005}_{-0.002}$	$0.002^{+0.002}_{-0.001}$	$0.004^{+0.005}_{-0.002}$
Fe^{12+}	$0.007^{+0.011}_{-0.004}$	$0.003^{+0.005}_{-0.002}$	$0.010^{+0.015}_{-0.006}$	$0.008^{+0.011}_{-0.005}$	$0.011^{+0.007}_{-0.004}$	$0.010^{+0.014}_{-0.006}$	$0.004^{+0.006}_{-0.002}$	$0.002^{+0.002}_{-0.001}$	$0.004^{+0.006}_{-0.002}$
Fe^{11+}	$0.016^{+0.016}_{-0.008}$	$0.008^{+0.012}_{-0.005}$	$0.018^{+0.016}_{-0.009}$	$0.017^{+0.014}_{-0.008}$	$0.020^{+0.007}_{-0.006}$	$0.017^{+0.014}_{-0.008}$	$0.012^{+0.019}_{-0.007}$	$0.004^{+0.003}_{-0.002}$	$0.012^{+0.015}_{-0.007}$
Fe^{10+}	$0.030^{+0.022}_{-0.012}$	$0.020^{+0.012}_{-0.007}$	$0.029^{+0.025}_{-0.014}$	$0.032^{+0.020}_{-0.012}$	$0.025^{+0.010}_{-0.007}$	$0.029^{+0.025}_{-0.013}$	$0.025^{+0.025}_{-0.013}$	$0.013^{+0.008}_{-0.005}$	$0.024^{+0.025}_{-0.012}$
Fe^{9+}	$0.036^{+0.029}_{-0.016}$	$0.026^{+0.011}_{-0.008}$	$0.032^{+0.036}_{-0.017}$	$0.039^{+0.028}_{-0.016}$	$0.018^{+0.015}_{-0.008}$	$0.035^{+0.034}_{-0.017}$	$0.033^{+0.027}_{-0.015}$	$0.027^{+0.010}_{-0.007}$	$0.032^{+0.024}_{-0.014}$
Fe^{8+}	$0.027^{+0.031}_{-0.015}$	$0.024^{+0.020}_{-0.011}$	$0.024^{+0.041}_{-0.015}$	$0.029^{+0.036}_{-0.016}$	$0.008^{+0.015}_{-0.005}$	$0.026^{+0.041}_{-0.016}$	$0.028^{+0.028}_{-0.014}$	$0.029^{+0.015}_{-0.010}$	$0.028^{+0.026}_{-0.013}$
Fe^{7+}	$0.007^{+0.012}_{-0.004}$	$0.006^{+0.008}_{-0.003}$	$0.007^{+0.016}_{-0.005}$	$0.007^{+0.013}_{-0.005}$	$0.001^{+0.003}_{-0.001}$	$0.007^{+0.016}_{-0.005}$	$0.008^{+0.013}_{-0.005}$	$0.008\ ^{+0.006}_{-0.004}$	$0.009^{+0.012}_{-0.005}$
Fe^{6+}	$0.002^{+0.005}_{-0.002}$	$0.001^{+0.002}_{-0.001}$	$0.002^{+0.005}_{-0.002}$	$0.002^{+0.005}_{-0.002}$	$0.001^{+0.001}_{-0.001}$	$0.002^{+0.005}_{-0.002}$	$0.004^{+0.007}_{-0.002}$	$0.002^{+0.002}_{-0.001}$	$0.003^{+0.004}_{-0.002}$

[a]Unavailable in the ACE database. Numbers are from Table 1 in SC00.

manuscript accepted in *SMILE Special Issue - Earth and Planetary Physics*

3 Atomic data

3.1 Velocity-dependent Cross-Sections

For the CX cross-sections we are using the compilation provided by the KRONOS[5] package at the University of Georgia (R. Cumbee et al., 2021). The KRONOS database includes comprehensive single electron cross-section values for many ion-neutral pairs, in particular H- and He-like charge states, and a wide range of collision energies. The calculations are based on the Multi-Channel Landau-Zener (MCLZ) approximation (Lyons et al., 2017). However, for several ion-neutral couples, other recommended data-sets based on more accurate methods, such as atomic-orbital close-coupling (AOCC; Fritsch & Lin, 1991), molecular-orbital close-coupling (MOCC; Janev et al., 1993; Harel et al., 1998), quantum-mechanical molecular-orbital close-coupling (QMOCC; Nolte et al., 2012) and classical trajectory Monte Carlo (CTMC; Abrines et al., 1966), are also provided. The KRONOS database package has been applied successfully on both solar system and astrophysical CX spectra (Mullen et al., 2017; R. S. Cumbee et al., 2016, 2017), and is also employed in the AtomDB Charge eXchange v2.0 (ACX2) spectral model (Smith et al., 2012, and http://www.atomdb.org/CX).

In this study, we use the velocity-dependent cross sections according to the KRONOS preferred order QMOCC → MOCC → AOCC → CTMC → MCLZ when available. The velocity-dependent cross sections from KRONOS are interpolated to the ACE He^{++} velocity time series. In short, this includes all the bare and He-like ions (C, N, O, Ne, Mg) and only a few Li-like, or lower charge states, of Ne, Mg, and S from table 2. If the cross-sections of any X^{q+}, M couple are not available through KRONOS, we use the SC00 cross-section values.

3.2 Emission Line Probabilities

The emission line probabilities (or yields) are based on two types of calculations, as described in Koutroumpa et al. (2006, 2009) and references therein.

For ions C, O, N, Ne, Mg the quantum yield cascades and emission line energies are calculated by Kharchenko (2005) for collisions with H and He respectively, and for the slow and fast SW regimes. These spectra have been successfully applied to cometary

[5] https://www.physast.uga.edu/ugacxdb/

SWCX emission spectra for slow and fast SW velocities (e.g., Kharchenko & Dalgarno, 2000, 2001; Rigazio et al., 2002; Kharchenko, 2005).

For heavier ions (Fe, Si, S, Mg), the quantum yield database was updated using the hydrogenic approximation (see details in Kharchenko, 2005; Koutroumpa et al., 2009) without distinction between H and He targets, or slow and fast SW regimes. Within this model, the exact positions of emission lines are not accurate compared to real emission spectra, but the total energy budget of the cascades in a given energy range is correct. Since many of those ion lines are blended with each other in the lower energy range (0.1-0.3 keV), this defect is less important at low to moderate spectral resolution of current instruments. However, future missions such as the Line Emission Mapper proposed concept (LEM; Kraft et al., 2022) and ESA's Athena mission (Barret et al., 2020), which will provide microcalorimeter-resolution data, will require a deep reevaluation of the spectral line ratios in the lower energy range. The complete spectral line database may be consulted in Koutroumpa (2007)[6].

4 Compound Cross-section Results

We calculate the compound cross-section α based on equation 3, where the $[\frac{X^{q+}}{p}]$ ratio is calculated as $[\frac{X^{q+}}{p}] = [\frac{X^{q+}}{O}][\frac{O}{He}][\frac{He}{p}]$, from the ACE SWICS and SWEPAM data presented previously[7]. Figure 6 shows the 27-day average values for the compound cross-sections with H and He in three energy ranges. We have chosen the full pass-band of SXI 0.1-2.0 keV, a slightly narrower band 0.3-2.0 keV that may be applied to the XMM-Newton PN and MOS detectors, and a very narrow band around the oxygen lines 0.5-0.7 keV. In Figure 7 we compare the α distributions (the histograms represent the number of occurrences) per solar wind type and solar activity period for these bands. In Table 3 we list the mode values of the distributions presented in Figure 7 for streamer, CH and ICME solar wind type for the complete ACE 1.1 database, as well as for the solar maximum

[6] https://tel.archives-ouvertes.fr/tel-00260160/document

[7] The combination of SWICS and SWEPAM data with respect to the He^{++} densities should be treated with caution, as the two instruments may have systematic differences, especially at the lower density regimes (e.g. CH). The SWEPAM n_{He} mode values are provided for comparison. Streamer: $0.135^{+0.196}_{-0.083}$, CH: $0.081^{+0.093}_{-0.045}$, ICME: $0.169^{+0.380}_{-0.119}$.

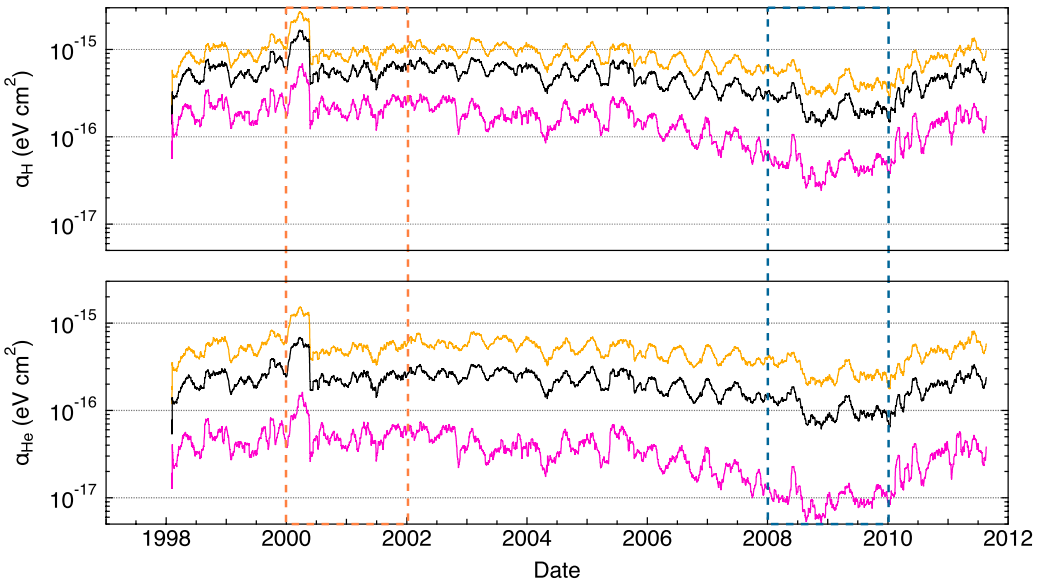

Figure 6: Top- Time series of the α_H for the 0.1 - 2.0 keV (yellow), 0.3 - 2.0 keV (black) and 0.5 - 0.7 keV (magenta) energy ranges. Bottom- Same as the top panel except for the α_{He}. All values are 27-day averages. The orange and blue dashed rectangles represent the solar maximum and solar minimum periods respectively.

and solar minimum periods. The uncertainties are again determined as the dispersion (width) of the distribution at half maximum.

During the full ACE 1.1 database period, the broad band calculations (0.1 - 2 keV) show little variations with the solar wind type, as it would be expected, since the blend of spectral lines of several ion charge states smooths out any individual variations. The values are of the same order as the Cravens et al. (2001) empirical value of 6×10^{-16} for photon energies > 0.1 keV. However, if we compare to the α calculated based on the SC00 charge-state abundances and cross-sections (Table 3), our values are more than 2 times lower. This is most probably due to the higher cross-sections used in the SC00 study, since we have demonstrated that the ion abundances are similar in most cases between the SC00 and ACE 1.1 analysis.

The α differences between solar wind types become more noticeable as the spectral range becomes narrower. The 0.5 - 0.7 keV band that includes mostly the oxygen lines (and some nitrogen) shows the most variability with a factor of 1.7 increase be-

tween streamer-type and ICME-type solar wind, and a factor of 4-6 lower for the CH-type compared to streamer.

Whittaker and Sembay (2016) had calculated α values for the 0.5 - 0.7 keV band based on the ACE O^{7+} and O^{8+} data. They split the solar wind data by velocity (with a cutoff at 500 km/s) and found modal values of 3.1×10^{-17} and 6.1×10^{-17} eV cm^2 for slow and fast solar wind respectively (red and blue vertical lines in the third panel of the first column in Figure 7 respectively). These values are inconsistent with the values we find in this analysis, and this may be for several reasons: (i) the velocity cutoff choice by Whittaker and Sembay (2016) in contrast with our selection criteria here, (ii) the fact that their calculations do not include the faint nitrogen lines around 0.5 keV as is the case in our analysis, and (iii) their use of cross-sections/line emission probabilities from Bodewits et al. (2007), which may be somewhat different from the ones considered here. However, we estimate that the most important reason for the difference in their values compared to ours is the use of linear bins/gaussian fits for their histograms of the α distributions instead of the logarithmic bins/log-normal distributions we employ here. Most puzzling is the fact that their fast (CH) solar wind α is higher than their slow (streamer) solar wind value, although they use oxygen charge-state abundances that are systematically less abundant in the fast solar wind. Moreover, in their table 1, the α value as a function of velocity shows a maximum of 8.2×10^{-17} eV cm^2 at 400 km/s. It is not clear to us what are the reasons for these inconsistencies.

The solar minimum values per solar wind type are systematically lower compared to solar maximum, which is in agreement with the depleted abundances found in the ACE data analysis in Section 2. The streamer population has a compound cross-section from 2 to 4.5 times higher in solar maximum compared to solar minimum depending on the energy band and neutral target. The CH population shows changes of a factor of 2 to 3, and the ICME population shows changes of a factor of 2.3 to 5.8.

It is also worth noting that in some occasions, in particular for the 0.1-2 keV band in solar maximum and solar minimum, the CH populations exhibit higher compound cross-sections compared to the streamer and ICME populations (Table 3). This is probably due to the fact that these bands are populated by spectral lines produced from source ions with lower charge-states (e.g. C^{5+}, O^{6+}) that are more abundant in the CH-type solar wind, as shown in Table 2. The decrease of higher q ions or increase in lower q ions

Table 3: Compound cross-sections of SWCX with H and He, in units of 10^{-16} eV cm^2, for streamer (Slow), CH (fast) and ICME solar wind for different solar activity periods. The uncertainties represent the dispersion (width) of the distribution at half maximum.

	Energy	Full period (1998-2011)			Max (2000-2002)			Min (2008-2010)		
	Range (keV)	Str.	CH	ICME	Str.	CH	ICME	Str.	CH	ICME
α_H	0.1 - 2.0	$7.8\ ^{+7.0}_{-3.7}$	$7.1^{+4.7}_{-2.9}$	$8.8^{+8.8}_{-4.4}$	$8.5^{+8.2}_{-4.3}$	$9.2^{+9.4}_{-4.6}$	$8.6^{+9.0}_{-4.5}$	$3.7^{+4.6}_{-2.1}$	$4.7^{+3.2}_{-1.7}$	$3.2^{+4.2}_{-1.8}$
	0.3 - 2.0	$4.5^{+4.3}_{-2.2}$	$3.2^{+2.3}_{-1.3}$	$5.6^{+6.2}_{-3.0}$	$5.0^{+4.9}_{-2.6}$	$4.6^{+5.3}_{-2.4}$	$5.6^{+6.2}_{-3.0}$	$1.9^{+2.8}_{-1.1}$	$2.0^{+1.3}_{-0.8}$	$1.7^{+2.3}_{-0.9}$
	0.5 - 0.7	$1.2^{+1.9}_{-7.5}$	$0.3^{+0.3}_{-0.1}$	$2.1^{+3.4}_{-1.3}$	$1.7^{+2.3}_{-1.0}$	$0.5^{+0.4}_{-0.2}$	$2.3^{+3.2}_{-1.4}$	$0.5^{+0.6}_{-0.3}$	$0.2^{+0.2}_{-0.1}$	$0.4^{+0.8}_{-0.3}$
α_{He}	0.1 - 2.0	$4.6\ ^{+4.2}_{-2.3}$	$4.8^{+3.0}_{-1.9}$	$4.7^{+5.2}_{-2.5}$	$4.9^{+5.0}_{-2.4}$	$6.2^{+5.5}_{-2.9}$	$4.5^{+4.8}_{-2.3}$	$2.3^{+2.9}_{-1.3}$	$3.2^{+2.1}_{-1.2}$	$2.0^{+2.6}_{-1.2}$
	0.3 - 2.0	$1.9^{+2.0}_{-1.0}$	$1.7^{+1.3}_{-0.7}$	$2.2^{+2.4}_{-1.2}$	$2.1^{+2.3}_{-1.1}$	$2.5^{+2.7}_{-1.3}$	$2.2^{+2.4}_{-1.1}$	$0.9^{+1.2}_{-0.5}$	$1.0^{+0.7}_{-0.4}$	$0.8^{+1.0}_{-0.4}$
	0.5 - 0.7	$0.3^{+0.4}_{-0.2}$	$0.05^{+0.07}_{-0.03}$	$0.5\ ^{+0.9}_{-0.3}$	$0.4^{+0.6}_{-0.2}$	$0.09^{+0.09}_{-0.04}$	$0.5^{+0.9}_{-0.3}$	$0.09^{+0.10}_{-0.06}$	$0.03^{+0.04}_{-0.02}$	$0.09^{+0.16}_{-0.06}$
$\alpha_{SC}^{(a)}$	0.1 - 2.0	22.8	12.2							
	0.3 - 2.0	16.2	6.8							
	0.5 - 0.7	8.9	1.3							

$^{(a)}$Calculated based on the $[\frac{X^{q+}}{O}]$ and cross-sections values from Table 1 in SC00.

for the CH wind, compared to streamer and ICME winds is stronger for lower Z elements and less apparent for higher Z elements. However, since the lower Z elements are generally more abundant than higher Z elements, and preferentially populate the lower energy portion of the spectrum, small effects in the ion ratios for the lower Z elements are seen more easily in the α values.

5 Conclusion

We have compiled ion charge state abundances from the ACE 1.1 database between 1998 and 2011, charge-exchange cross-sections from the KRONOS database, and line emission probabilities from literature. We have calculated the compound cross-sections α for charge-exchange collisions with H and He atoms for broad (0.1 - 2 keV), average (0.3 - 2 keV) and narrow (0.5 - 0.7 keV) spectral ranges, for streamer, CH and ICME solar wind types and in different solar cycle periods.

We find that for broad band ranges (0.1 - 2 keV), there is little variation in α for the different solar wind types in each solar period. The distinction between solar wind types becomes significant as we narrow down the spectral band to single ion emission range, such as the oxygen band (0.5 - 0.7 keV). This is consistent with previous studies showing that the SWCX signal is more influenced by individual ion variations when analysing bands where only few ions dominate the spectrum, as opposed to broad bands where blends of many ion spectral lines are measured (Kuntz et al., 2015). Most notably, we find variations between solar maximum and solar minimum periods for each solar wind type separately, due to sharp changes in ion abundances measured by ACE/SWICS, as demonstrated in this and previous studies (Lepri et al., 2013).

Using the compound cross-sections in broad X-ray bands is a convenient method to quickly link the SWCX signal in magnetospheric calculations with global increases of solar wind proton flux. However, it has been demonstrated in previous studies that the individual ion abundances may impact the SWCX signal in a more significant way (e.g., Y. Zhang et al., 2022). Therefore it is important to combine several approaches allowing for quick analyses of the magnetosphere's dynamic response (e.g. with MHD models), and more detailed modeling focusing on individual ions and the way they evolve around the magnetospheric boundaries, or precipitate through the cusps (e.g. with test-particle models). The SMILE/SXI instrument has both a broad energy range (0.1 - 2

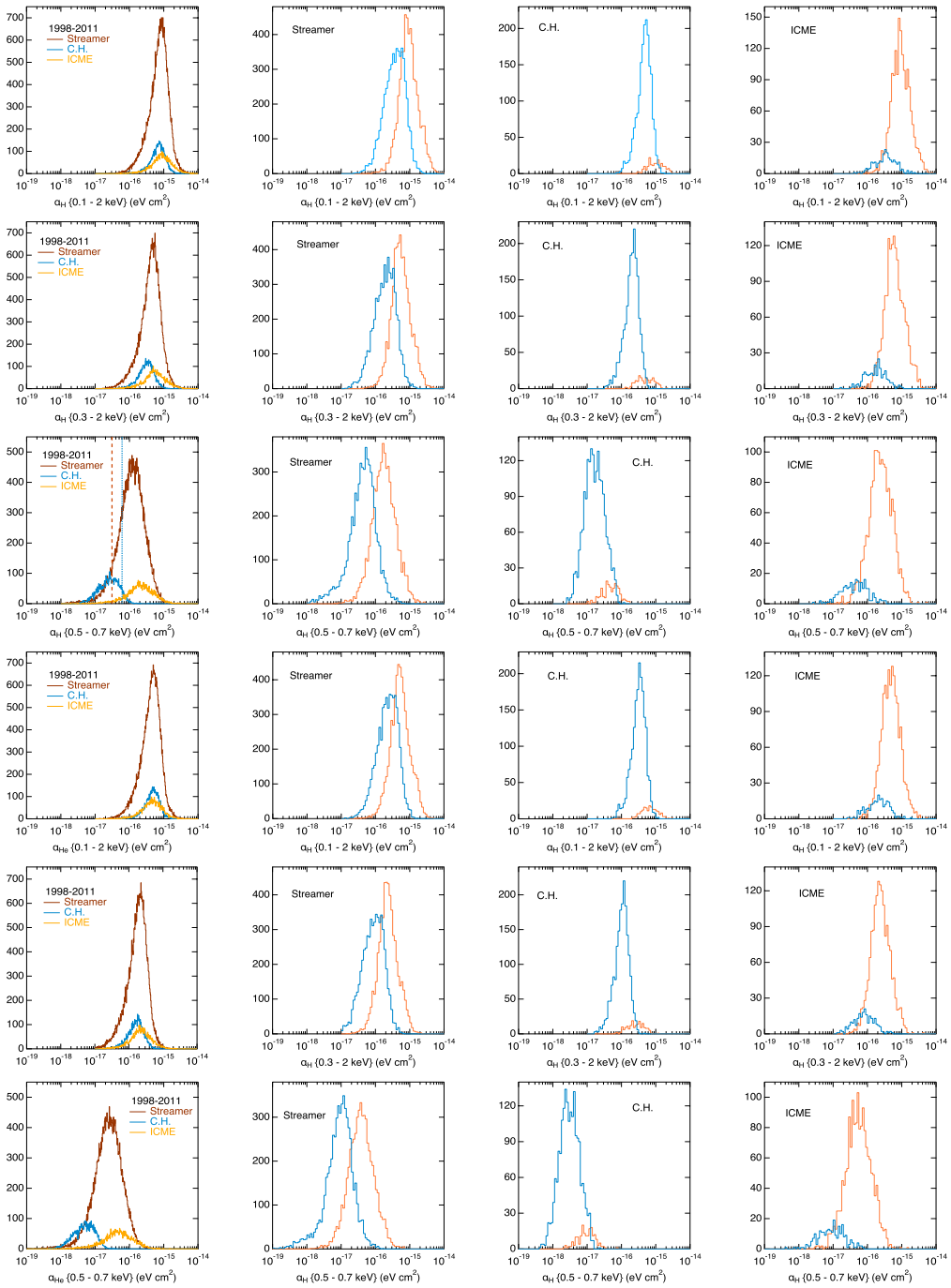

Figure 7: From top to bottom, histograms (in number of occurrences) for the α_H 0.1-2 keV, 0.3-2 keV, 0.5-0.7 keV range, and for the α_{He} 0.1-2 keV, 0.3-2 keV, 0.5-0.7 keV range. The first column includes histograms for streamer (dark red), coronal hole (blue) and ICME (yellow) SW for the complete ACE 1.1 database (1998-2011). The second, third and fourth columns include histograms for the streamer, C.H. and ICME types of SW respectively, separated in solar maximum (orange) and solar minimum (blue). The red and blue vertical lines in panel three of the first column correspond to the Whittaker and Sembay (2016) values for the same energy range.

keV) and enough spectroscopic resolution to separate several strong lines (e.g. from O, C, N and Ne ions), and will certainly benefit from these combined approaches.

In that context, and in view of future X-ray missions (e.g., LEM, ATHENA) that will provide high-resolution spectra of the SWCX emission in the 0.1 - 2 keV range, it is crucial to improve developments in two areas. First, we need to improve the databases of cross-sections and emission probabilities for complex ion structures, such as the ions Mg, Si, S, Fe, populating the low-energy band 0.1 - 0.3 keV. For this, we need accurate quantum calculations, corroborated by experimental measurements in collision energies similar to astrophysical conditions. In addition, continuous monitoring of the solar wind ion composition is a key link between the solar wind effects through interplanetary space and in approach of the magnetosphere to the SWCX signal measured near the magnetospheric boundaries and the cusps. With the declining performances of ACE/SWICS since 2011, it becomes imperative that new missions allowing for monitoring the solar wind ion composition are developed and, if possible, launched in tandem with X-ray observatories.

Acknowledgments

This work was supported by CNES. I wish to thank the SWEPAM and SWICS instrument teams for providing the ACE data through the ACE Science Center: http://www.srl.caltech.edu/ACE/ASC/ind
I am grateful to Sue Lepri, Jim Raines, Ruedi von Steiger and Liang Zhao for invaluable discussions on the SWICS composition data. I am very thankful to Renata Cumbee for her advice on the use of the cross sections in the KRONOS charge transfer database. I cannot omit to thank Vasili Kharchenko for always happily answering my endless questions on line emission probabilities. Finally, I deeply appreciate the two referees' thorough evaluations that greatly improved this paper.

References

Abrines, R., Percival, I. C., Abrines, R., & Percival, I. C. (1966). Classical theory of charge transfer and ionization of hydrogen atoms by protons. *PPS*, *88*, 861-872. Retrieved from `https://ui.adsabs.harvard.edu/abs/1966PPS....88..861A/abstract` doi: 10.1088/0370-1328/88/4/306

Barret, D., Decourchelle, A., Fabian, A., Guainazzi, M., Nandra, K., Smith, R., & den Herder, J. W. (2020, 2). The athena space x-ray observatory and the

astrophysics of hot plasma†. *Astronomische Nachrichten*, *341*, 224-235. Retrieved from https://ui.adsabs.harvard.edu/abs/2020AN....341..224B/abstract doi: 10.1002/asna.202023782

Bodewits, D., Christian, D. J., Torney, M., Dryer, M., Lisse, C. M., Dennerl, K., ... Hoekstra, R. (2007, apr). Spectral Analysis of the Chandra Comet Survey. *Astronomy and Astrophysics, Volume 469, Issue 3, July III 2007, pp.1183-1195*, *469*, 1183–1195. Retrieved from http://arxiv.org/abs/0704.1648http://dx.doi.org/10.1051/0004-6361:20077410 doi: 10.1051/0004-6361:20077410

Branduardi-Raymont, G., Bhardwaj, A., Elsner, R. F., Gladstone, G. R., Ramsay, G., Rodriguez, P., ... Cravens, T. E. (2007, 2). A study of jupiter's aurorae with xmm-newton. *Astronomy and Astrophysics*, *463*, 761-774. Retrieved from http://adsabs.harvard.edu/abs/2007A&A...463..761B doi: 10.1051/0004-6361:20066406

Branduardi-Raymont, G., Wang, C., Escoubet, C., Adamovic, M., Agnolon, D., Berthomier, M., ... Zhu, Z. (2018). *SMILE Solar wind Magnetosphere Ionosphere Link Explorer Definition Study Report European Space Agency* (Tech. Rep.). Retrieved from https://sci.esa.int/documents/35028/36141/1567260374869-SMILE_RedBook_ESA_SCI_2018_1.pdf

Carter, J. A., Sembay, S., & Read, A. M. (2009, 11). A high charge state coronal mass ejection seen through solar wind charge exchange emission as detected by xmm-newton. *Monthly Notices of the Royal Astronomical Society*, *402*, 867-878. Retrieved from https://academic.oup.com/mnras/article-lookup/doi/10.1111/j.1365-2966.2009.15985.xhttp://arxiv.org/abs/0911.0897http://dx.doi.org/10.1111/j.1365-2966.2009.15985.x doi: 10.1111/j.1365-2966.2009.15985.x

Connor, H. K., Sibeck, D. G., Collier, M. R., Baliukin, I. I., Branduardi-Raymont, G., Brandt, P. C., ... Zoennchen, J. H. (2021, mar). Soft X-ray and ENA Imaging of the Earth's Dayside Magnetosphere. *Journal of Geophysical Research: Space Physics*, *126*(3), e28816. Retrieved from https://onlinelibrary.wiley.com/doi/10.1029/2020JA028816 doi: 10.1029/2020JA028816

Cox, D. P. (1998). *The local bubble and beyond lyman-spitzer-colloquium*

(Vol. 506; D. Breitschwerdt, M. Freyberg, & J. Trümper, Eds.). Springer Berlin Heidelberg. Retrieved from http://adsabs.harvard.edu/abs/1998LNP...506..121C doi: 10.1007/BFb0104684

Cravens, T. E. (1997). Comet Hyakutake x-ray source: Charge transfer of solar wind heavy ions. *Geophysical Research Letters*, *24*(1), 105. Retrieved from http://adsabs.harvard.edu/abs/1997GeoRL..24..105C doi: 10.1029/96GL03780

Cravens, T. E. (2000, 4). Heliospheric x-ray emission associated with charge transfer of the solar wind with interstellar neutrals. *The Astrophysical Journal*, *532*, L153-L156. Retrieved from http://adsabs.harvard.edu/abs/2000ApJ...532L.153C doi: 10.1086/312574

Cravens, T. E., Howell, E., Waite, J. H., & Gladstone, G. R. (1995, September). Auroral oxygen precipitation at Jupiter. *Journal of Geophysical Research*, *100*(A9), 17153-17162. doi: 10.1029/95JA00970

Cravens, T. E., Robertson, I. P., & Snowden, S. L. (2001). Temporal variations of geocoronal and heliospheric x-ray emission associated with the solar wind interaction with neutrals. *Journal of Geophysical Research*, *106*, 24883-24892. Retrieved from http://adsabs.harvard.edu/abs/2001JGR...10624883C doi: 10.1029/2000JA000461

Cumbee, R., Stancil, P., & Mcilvane, S. (2021, jun). The Interactive Kronos Charge Exchange Database. *American Astronomical Society meeting 238, id. 126.01. Bulletin of the American Astronomical Society, Vol. 53, No. 6 e-id 2021n6i126p01*, *53*(6), 126.01. Retrieved from https://ui.adsabs.harvard.edu/abs/2021AAS...23812601C/abstract

Cumbee, R. S., Liu, L., Lyons, D., Schultz, D. R., Stancil, P. C., Wang, J. G., & Ali, R. (2016, 3). Ne x x-ray emission due to charge exchange in m82. *MNRAS*, *458*, 3554-3560. Retrieved from http://arxiv.org/abs/1603.04907http://dx.doi.org/10.1093/mnras/stw527 doi: 10.1093/mnras/stw527

Cumbee, R. S., Mullen, P. D., Lyons, D., Shelton, R. L., Fogle, M., Schultz, D. R., & Stancil, P. C. (2017, dec). Charge Exchange X-Ray Emission due to Highly Charged Ion Collisions with H, He, and H 2 : Line Ratios for Heliospheric and Interstellar Applications. *The Astrophysical Journal*, *852*(1), 7. Retrieved from https://iopscience.iop.org/article/10.3847/1538-4357/aa99d8 doi: 10.3847/1538-4357/aa99d8

Dennerl, K. (2002, 11). Discovery of x-rays from mars with chandra. *Astronomy and Astrophysics*, *394*, 1119-1128. Retrieved from http://adsabs.harvard.edu/abs/2002A&A...394.1119D doi: 10.1051/0004-6361:20021116

Dennerl, K., Burwitz, V., Englhauser, J., Lisse, C., & Wolk, S. (2002, 4). Discovery of x?rays from venus with chandra. *Astronomy and Astrophysics*, *386*, 319-330. Retrieved from http://adsabs.harvard.edu/abs/2002A&A...386..319D doi: 10.1051/0004-6361:20020097

Dennerl, K., Englhauser, J., & Trümper, J. (1997, September). X-ray emissions from comets detected in the Röntgen X-ray satellite all-sky survey. *Science*, *277*(5332), 1625-1630. doi: 10.1126/science.277.5332.1625

Freyberg, M. J. (1998). On the Zero-Level of the Soft X-ray Background. In D. Breitschwerdt, M. J. Freyberg, & J. Truemper (Eds.), *Iau colloq. 166: The local bubble and beyond* (Vol. 506, p. 113-116). doi: 10.1007/BFb0104704

Fritsch, W., & Lin, C. (1991). The semiclassical close-coupling description of atomic collisions: Recent developments and results. *Physics Reports*, *202*(1), 1-97. Retrieved from https://www.sciencedirect.com/science/article/pii/037015739190008A doi: https://doi.org/10.1016/0370-1573(91)90008-A

Gloeckler, G., Cain, J., Ipavich, F., Tums, E., Bedini, P., Fisk, L., ... Kallenbach, R. (1998, jul). Investigation of the composition of solar and interstellar matter using solar wind and pickup ion measurements with SWICS and SWIMS on the ACE spacecraft. *Space Science Reviews*, *86*(1/4), 497–539. Retrieved from http://link.springer.com/10.1023/A:1005036131689 doi: 10.1023/A:1005036131689

Harel, C., Jouin, H., & Pons, B. (1998, 3). Cross sections for electron capture from atomic hydrogen by fully stripped ions in the 0.05–1.00 a.u. impact velocity range. *Atomic Data and Nuclear Data Tables*, *68*, 279-302. Retrieved from http://adsabs.harvard.edu/abs/1998ADNDT..68..279H doi: 10.1006/adnd.1997.0768

Hu, Y. Q., Guo, X. C., & Wang, C. (2007). On the ionospheric and reconnection potentials of the earth: Results from global mhd simulations. *Journal of Geophysical Research: Space Physics*, *112*(A7). Retrieved from https://agupubs.onlinelibrary.wiley.com/doi/abs/10.1029/2006JA012145 doi: https://doi.org/10.1029/2006JA012145

Ishi, D., Ishikawa, K., Numazawa, M., Miyoshi, Y., Terada, N., Mitsuda, K., ... Ishikawa, K. (2019, 2). Suzaku detection of enigmatic geocoronal solar wind charge exchange event associated with coronal mass ejection. *Publications of the Astronomical Society of Japan*, *71*, 791. Retrieved from https://academic.oup.com/pasj/article/doi/10.1093/pasj/psy142/5281180http://arxiv.org/abs/1902.07652http://dx.doi.org/10.1093/pasj/psy142 doi: 10.1093/pasj/psy142

Issautier, K., Chat, G. L., Meyer-Vernet, N., Moncuquet, M., Hoang, S., MacDowall, R. J., & McComas, D. J. (2008, 10). Electron properties of high-speed solar wind from polar coronal holes obtained by ulysses thermal noise spectroscopy: Not so dense, not so hot. *Geophysical Research Letters*, *35*, L19101. Retrieved from http://doi.wiley.com/10.1029/2008GL034912 doi: 10.1029/2008GL034912

Janev, R. K., Phaneuf, R. A., Tawara, H., & Shirai, T. (1993). Recommended cross sections for state-selective electron capture in collisions of c¡sup¿6+¡/sup¿ and o¡sup¿8+¡/sup¿ ions with atomic hydrogen. *ADNDT*, *55*, 201-232. Retrieved from https://ui.adsabs.harvard.edu/abs/1993ADNDT..55..201J/abstract doi: 10.1006/ADND.1993.1021

Kharchenko, V. (2005). Charge-Exchange Mechanism of X-ray Emission. In *Aip conference proceedings* (Vol. 774, pp. 271–280). AIP. Retrieved from http://adsabs.harvard.edu/abs/2005AIPC..774..271K doi: 10.1063/1.1960938

Kharchenko, V., & Dalgarno, A. (2000, aug). Spectra of cometary X rays induced by solar wind ions. *Journal of Geophysical Research: Space Physics*, *105*(A8), 18351–18359. Retrieved from http://adsabs.harvard.edu/abs/2000JGR...10518351Khttp://doi.wiley.com/10.1029/1999JA000203 doi: 10.1029/1999JA000203

Kharchenko, V., & Dalgarno, A. (2001, jun). Variability of Cometary X-Ray Emission Induced by Solar Wind Ions. *The Astrophysical Journal*, *554*(1), L99–L102. Retrieved from http://adsabs.harvard.edu/abs/2001ApJ...554L..99K

Koutroumpa, D. (2007, 11). X-ray and uv gas emission and charge-exchange phenomena in the heliosphere: application to various astrophysical systems. *PhD Thesis, Université Pierre et Marie Curie - Paris 6, 2007*. Retrieved from

https://ui.adsabs.harvard.edu/abs/2007PhDT.....456K/abstract

Koutroumpa, D., Lallement, R., & Kharchenko, V. (2009, August). The Spectrum of the Solar Wind Charge Exchange Emission: Contribution to the Soft X-ray Background. In R. K. Smith, S. L. Snowden, & K. D. Kuntz (Eds.), *The local bubble and beyond ii* (Vol. 1156, p. 62-73). doi: 10.1063/1.3211835

Koutroumpa, D., Lallement, R., Kharchenko, V., Dalgarno, A., Pepino, R., Izmodenov, V., & Quémerais, E. (2006, dec). Charge-transfer induced EUV and soft X-ray emissions in the heliosphere. *Astronomy and Astrophysics*, *460*(1), 289–300. Retrieved from http://adsabs.harvard.edu/abs/2006A&A...460..289K doi: 10.1051/0004-6361:20065250

Kraft, R., Markevitch, M., Kilbourne, C., Adams, J. S., Akamatsu, H., Ayromlou, M., ... Zuhone, J. (2022). *Line emission mapper probing physics of cosmic ecosystems a mission concept for the nasa 2023 astrophysics probes ao.*

Kuntz, K. D. (2018, nov). Solar Wind Charge Exchange: An Astrophysical Nuisance. *The Astronomy and Astrophysics Review, Volume 27, Issue 1, article id. 1, 71 pp.*, *27*. Retrieved from http://arxiv.org/abs/1811.06454http://dx.doi.org/10.1007/s00159-018-0114-0 doi: 10.1007/s00159-018-0114-0

Kuntz, K. D., Collado-Vega, Y. M., Collier, M. R., Connor, H. K., Cravens, T. E., Koutroumpa, D., ... Walsh, B. M. (2015, jul). THE SOLAR WIND CHARGE-EXCHANGE PRODUCTION FACTOR FOR HYDROGEN. *The Astrophysical Journal*, *808*(2), 143. Retrieved from https://iopscience.iop.org/article/10.1088/0004-637X/808/2/143 doi: 10.1088/0004-637X/808/2/143

Lallement, R. (2004, 4). The heliospheric soft x-ray emission pattern during the rosat survey: Inferences on local bubble hot gas. *Astronomy and Astrophysics*, *418*, 143-150. Retrieved from http://adsabs.harvard.edu/abs/2004A&A...418..143L doi: 10.1051/0004-6361:20040059

Lepri, S. T., Landi, E., & Zurbuchen, T. H. (2013, apr). SOLAR WIND HEAVY IONS OVER SOLAR CYCLE 23: ACE /SWICS MEASUREMENTS. *The Astrophysical Journal*, *768*(1), 94. Retrieved from http://stacks.iop.org/0004-637X/768/i=1/a=94?key=crossref.54b89c9f9395f0b3a2501663287f6dd9 doi: 10.1088/0004-637X/768/1/94

Lisse, C. M., Dennerl, K., Englhauser, J., Harden, M., Marshall, F. E., Mumma,

M. J., ... West, R. G. (1996, oct). Discovery of X-ray and Extreme Ultraviolet Emission from Comet C/Hyakutake 1996 B2. *Science*, *274*(5285), 205–209. Retrieved from `http://adsabs.harvard.edu/abs/1996Sci...274..205L` doi: 10.1126/science.274.5285.205

Lisse, C. M., McNutt, R. L., Wolk, S. J., Bagenal, F., Stern, S. A., Gladstone, G. R., ... Ennico, K. A. (2017). The puzzling detection of x-rays from pluto by chandra. *Icarus*, *287*. doi: 10.1016/j.icarus.2016.07.008

Lyons, D., Cumbee, R. S., & Stancil, P. C. (2017, oct). Charge Exchange of Highly Charged Ne and Mg Ions with H and He. *The Astrophysical Journal Supplement Series*, *232*(2), 27. Retrieved from `https://iopscience.iop.org/article/10.3847/1538-4365/aa8d16` doi: 10.3847/1538-4365/aa8d16

Modolo, R., Hess, S., Mancini, M., Leblanc, F., Chaufray, J.-Y., Brain, D., ... Mazelle, C. (2016, July). Mars-solar wind interaction: LatHyS, an improved parallel 3-D multispecies hybrid model. *Journal of Geophysical Research (Space Physics)*, *121*(7), 6378-6399. doi: 10.1002/2015JA022324

Mullen, P. D., Cumbee, R. S., Lyons, D., Gu, L., Kaastra, J., Shelton, R. L., & Stancil, P. C. (2017, jul). Line Ratios for Solar Wind Charge Exchange with Comets. *The Astrophysical Journal*, *844*(1), 7. Retrieved from `https://iopscience.iop.org/article/10.3847/1538-4357/aa7752` doi: 10.3847/1538-4357/aa7752

Nolte, J. L., Stancil, P. C., Liebermann, H. P., Buenker, R. J., Hui, Y., Schultz, D. R., ... Schultz, D. R. (2012, 12). Final-state-resolved charge exchange in c¡sup¿5 +¡/sup¿ collisions with h. *JPhB*, *45*, 245202. Retrieved from `https://ui.adsabs.harvard.edu/abs/2012JPhB...45x5202N/abstract` doi: 10.1088/0953-4075/45/24/245202

Pepino, R., Kharchenko, V., Dalgarno, A., Lallement, R., Pepino, R., Kharchenko, V., ... Lallement, R. (2004, dec). Spectra of the X-Ray Emission Induced in the Interaction between the Solar Wind and the Heliospheric Gas. *The Astrophysical Journal*, *617*(2), 1347–1352. Retrieved from `https://iopscience.iop.org/article/10.1086/425682` doi: 10.1086/425682

Raeder, J., McPherron, R. L., Frank, L. A., Kokubun, S., Lu, G., Mukai, T., ... Slavin, J. A. (2001). Global simulation of the geospace environment modeling substorm challenge event. *Journal of Geophysical Re-*

search: Space Physics, *106*(A1), 381-395. Retrieved from https://agupubs.onlinelibrary.wiley.com/doi/abs/10.1029/2000JA000605 doi: https://doi.org/10.1029/2000JA000605

Richardson, I. G., & Cane, H. V. (2004, sep). Identification of interplanetary coronal mass ejections at 1 AU using multiple solar wind plasma composition anomalies. *Journal of Geophysical Research*, *109*(A9), A09104. Retrieved from http://doi.wiley.com/10.1029/2004JA010598 doi: 10.1029/2004JA010598

Rigazio, M., Kharchenko, V., Dalgarno, A., Rigazio, M., Kharchenko, V., & Dalgarno, A. (2002, dec). X-ray emission spectra induced by hydrogenic ions in charge transfer collisions. *Physical Review A*, *66*(6), 064701. Retrieved from https://link.aps.org/doi/10.1103/PhysRevA.66.064701 doi: 10.1103/PhysRevA.66.064701

Robertson, I. P., & Cravens, T. E. (2003, April). X-ray emission from the terrestrial magnetosheath. *Geophysical Research Letters*, *30*(8), 1439. doi: 10.1029/2002GL016740

Schwadron, N. A., & Cravens, T. E. (2000, nov). Implications of Solar Wind Composition for Cometary X-Rays. *The Astrophysical Journal*, *544*(1), 558–566. Retrieved from http://adsabs.harvard.edu/abs/2000ApJ...544..558S doi: 10.1086/317176

Sibeck, D., Allen, R., Aryan, H., Bodewits, D., Brandt, P., Branduardi-Raymont, G., ... Wing, S. (2018). Imaging Plasma Density Structures in the Soft X-Rays Generated by Solar Wind Charge Exchange with Neutrals. *Space Science Reviews*, *214*(4). doi: 10.1007/s11214-018-0504-7

Smith, R. K., Foster, A. R., & Brickhouse, N. S. (2012, April). Approximating the X-ray spectrum emitted from astrophysical charge exchange. *Astronomische Nachrichten*, *333*(4), 301. doi: 10.1002/asna.201211673

Snowden, S. L., Collier, M. R., & Kuntz, K. D. (2004, aug). XMM-Newton Observation of Solar Wind Charge Exchange Emission. *The Astrophysical Journal*, *610*(2), 1182–1190. Retrieved from http://adsabs.harvard.edu/abs/2004ApJ...610.1182S doi: 10.1086/421841

Snowden, S. L., McCammon, D., Burrows, D. N., & Mendenhall, J. A. (1994, 4). Analysis procedures for rosat xrt/pspc observations of extended objects

and the diffuse background. *The Astrophysical Journal*, *424*, 714. Retrieved from http://adsabs.harvard.edu/abs/1994ApJ...424..714S doi: 10.1086/173925

Sun, T. R., Wang, C., Sembay, S. F., Lopez, R. E., Escoubet, C. P., Branduardi-Raymont, G., ... Guo, Y. H. (2019, apr). Soft X-ray Imaging of the Magnetosheath and Cusps Under Different Solar Wind Conditions: MHD Simulations. *Journal of Geophysical Research: Space Physics*, *124*(4), 2018JA026093. Retrieved from https://onlinelibrary.wiley.com/doi/abs/10.1029/2018JA026093 doi: 10.1029/2018JA026093

Tkachenko, Y., Koutroumpa, D., Modolo, R., Connor, H., & Sembay, S. (2021, dec). Charge exchange X-ray emission in the near-Earth environment: Simulations in preparation for the SMILE magnetospheric mission. *SF2A-2021: Proceedings of the Annual meeting of the French Society of Astronomy and Astrophysics. Eds.: A. Siebert, K. Baillié, E. Lagadec, N. Lagarde, J. Malzac, J.-B. Marquette, M. N'Diaye, J. Richard, O. Venot, 2021, pp.487-490*, 487. Retrieved from https://ui.adsabs.harvard.edu/abs/2021sf2a.conf..487T/abstract

von Steiger, R., & Zurbuchen, T. H. (2015, dec). SOLAR METALLICITY DERIVED FROM IN SITU SOLAR WIND COMPOSITION. *The Astrophysical Journal*, *816*(1), 13. Retrieved from https://iopscience.iop.org/article/10.3847/0004-637X/816/1/13 doi: 10.3847/0004-637X/816/1/13

Walsh, B., Collier, M. R., Busk, S., Connor, H. K., Kuntz, K. D., McShane, J., ... Thomas, N. (2020). The Lunar Environment Heliospheric X-ray Imager (LEXI) - A mission for global magnetospheric imaging. *AGUFM*, *2020*, SM029–01. Retrieved from https://ui.adsabs.harvard.edu/abs/2020AGUFMSM029..01W/abstract

Wegmann, R., Schmidt, H., Lisse, C., Dennerl, K., & Englhauser, J. (1998, 5). X-rays from comets generated by energetic solar wind particles. *Planetary and Space Science*, *46*, 603-612. Retrieved from http://adsabs.harvard.edu/abs/1998P%26SS...46..603W doi: 10.1016/S0032-0633(97)00196-7

Whittaker, I. C., & Sembay, S. (2016, jul). A comparison of empirical and experimental O 7+ , O 8+ , and O/H values, with applications to terrestrial solar wind charge exchange. *Geophysical Research Letters*, *43*(14), 7328–

7337. Retrieved from http://doi.wiley.com/10.1002/2016GL069914 doi: 10.1002/2016GL069914

Zhang, J., Woch, J., K., S. S., von Steiger, R., & Forsyth, R. (2003). Interplanetary and solar surface properties of coronal holes observed during solar maximum. *Journal of Geophysical Research*, *108*. doi: 10.1029/2002JA009538

Zhang, Y., Sun, T., Wang, C., Ji, L., Carter, J. A., Sembay, S., ... Zhao, X. (2022, 6). Solar wind charge exchange soft x-ray emissions in the magnetosphere during an interplanetary coronal mass ejection compared to its driven sheath. *The Astrophysical Journal Letters*, *932*, L1. Retrieved from https://iopscience.iop.org/article/10.3847/2041-8213/ac7521 doi: 10.3847/2041-8213/ac7521

Zhao, L., Landi, E., Lepri, S. T., & Carpenter, D. (2022, jul). Depletion of Heavy Ion Abundances in Slow Solar Wind and Its Association with Quiet Sun Regions. *Universe*, *8*(8), 393. Retrieved from https://www.mdpi.com/2218-1997/8/8/393 doi: 10.3390/universe8080393

Zhao, L., Landi, E., Lepri, S. T., Kocher, M., Zurbuchen, T. H., Fisk, L. A., & Raines, J. M. (2017, jan). AN ANOMALOUS COMPOSITION IN SLOW SOLAR WIND AS A SIGNATURE OF MAGNETIC RECONNECTION IN ITS SOURCE REGION. *The Astrophysical Journal Supplement Series*, *228*(1), 4. Retrieved from https://iopscience.iop.org/article/10.3847/1538-4365/228/1/4 doi: 10.3847/1538-4365/228/1/4

Zhao, L., Zurbuchen, T. H., Fisk, L. A., Zhao, L., Zurbuchen, T. H., & Fisk, L. A. (2009, jul). Global distribution of the solar wind during solar cycle 23: ACE observations. *Geophysical Research Letters*, *36*(14), L14104. Retrieved from http://doi.wiley.com/10.1029/2009GL039181 doi: 10.1029/2009GL039181